Research Square

Preprints are preliminary reports that have not undergone peer review.
They should not be considered conclusive, used to inform clinical practice,
or referenced by the media as validated information.

Self-organized Ag-Sb lamellae redirect cracks in all-solid-state Li metal batteries

Hongli Zhu

h.zhu@neu.edu

Northeastern University https://orcid.org/0000-0003-1733-4333

Cheng Xu

Northeastern University

Shiyao Lin

University of Texas at Arlington

Bharat Pant

University of Texas Arlington https://orcid.org/0000-0002-2912-0319

Ye Cao

University of Texas Arlington https://orcid.org/0000-0002-7365-7447

Jiwei Wang

Northeastern University

Han Su

University of Maryland, College Park https://orcid.org/0009-0006-1103-3774

Hua Zhou

Argonne National Laboratory https://orcid.org/0000-0001-9642-8674

Luxi Li

Argonne National Laboratory https://orcid.org/0000-0002-9259-8796

Xianhui Zhao

Oak Ridge National Laboratory https://orcid.org/0000-0002-0282-5810

Ercan Cakmak

Oak Ridge National Laboratory

Longqing Chen

The Pennsylvania State University https://orcid.org/0000-0003-3359-3781

Chunsheng Wang

University of Maryland, College Park https://orcid.org/0000-0002-8626-6381

Article

Keywords: Self-organized lamellar interface, crack redirection, Li metal batteries, all-solid-state batteries, Li dendrite, Li-sulfur batteries

Posted Date: August 20th, 2026

DOI: https://doi.org/10.21203/rs.3.rs-10627954/v1

License: This work is licensed under a Creative Commons Attribution 4.0 International License.
Read Full License

Additional Declarations: There is **NO** Competing Interest.

Self-organized Ag-Sb lamellae redirect cracks in all-solid-state Li metal batteries

Cheng Xu,[1] Shiyao Lin,[2] Bharat Pant,[3] Ye Cao,[3] Jiwei Wang,[1] Han Su,[4] Hua Zhou,[5] Luxi Li,[5] Xianhui Zhao,[6] Ercan Cakmak,[6] Longqing Chen,[7] Chunsheng Wang,*[,4] Hongli Zhu*[,1]

[1]Department of Mechanical and Industrial Engineering, Northeastern University, Boston, MA 02115, USA

[2]Department of Mechanical and Aerospace Engineering, University of Texas at Arlington, Arlington, TX 76019, United States

[3]Department of Materials Science and Engineering, University of Texas at Arlington, Arlington, TX 76019, United States

[4]Department of Chemical and Biomolecular Engineering, University of Maryland, College Park, MD 20740, USA

[5]X-ray Science Division, Advanced Photon Source, Argonne National Laboratory, Lemont, IL 60439, USA.

[6]Oak Ridge National Laboratory, Oak Ridge, TN 37830, USA

[7]Department of Materials Science and Engineering, The Pennsylvania State University, University Park, Pennsylvania 16802, USA

Corresponding authors: h.zhu@neu.edu; cswang@umd.edu

Abstract

Interfacial instability and crack-assisted lithium (Li) dendrite propagation limit the practical deployment of all-solid-state Li metal batteries. Applying stack pressure improves interfacial contact but also accelerates through-thickness crack propagation without stabilizing the Li/solid-electrolyte interface. Here, we overcome this intrinsic tradeoff by using an in-situ generated self-organized Ag-Sb lamellar interlayer at the Li/solid electrolyte interface that continuously redirects crack propagation and Li growth parallel to the electrode. Sequential lithiation of Sb- and Ag-rich phases produces alternating Li_3Sb- and Li_2AgSb-rich lamellae due to lattice-mismatch strain. Synchrotron X-ray tomography, electron microscopy, finite-element and phase-field modelling reveal that through-thickness cracks are redirected into lateral cracks along the lamellar phase, limiting Li penetration into the solid electrolyte. Consequently, symmetric cells operate up to 9.0 mA cm^{-2} at 9.0 mAh cm^{-2}, while Li-S cells cycle stably at 4.91 mAh cm^{-2}, whereas cells without the interlayer short-circuit during the first charging cycle. These findings establish a cycling-adaptive self-organized interfacial strategy that suppresses dendrites through crack redirection rather than direct mechanical blocking.

Keywords: Self-organized lamellar interface, crack redirection, Li metal batteries, all-solid-state batteries, Li dendrite, Li-sulfur batteries

Li metal is the ideal anode for high-energy solid-state batteries. Yet, its coupling with solid electrolytes (SEs) introduces a fundamentally different mechanical failure mode from that in liquid-electrolyte batteries.[1,2] During Li plating, pre-existing defects promote Li filament growth, which initiates and propagates cracks through the SE, eventually forming through-thickness cracks from the anode to the cathode and leading to cell failure.[3] Operando stress measurements further revealed that crack propagation is governed by coupled electrochemical-mechanical processes during cycling, providing mechanistic insight into solid-state battery failure.[4] During Li stripping, interfacial Li depletion generates voids that amplify local current density during subsequent deposition, further promoting Li penetration. Although stack pressure suppresses void formation and maintains intimate interfacial contact,[5] it also drives through-thickness crack propagation, leading to short circuiting.[6,7]

To suppress short-circuiting from Li dendrite growth, controlling crack growth direction has recently emerged as an effective strategy to mitigate crack-driven Li dendrite growth in Li metal

solid-state batteries.[7,8] To suppress cracks, one representative strategy employs a Li_6PS_5Cl/ $Li_{10}GeP_2S_{12}$/Li_6PS_5Cl tri-layer electrolyte architecture, in which the different mechanical properties of the tri-layers suppress crack propagation across the electrolyte,[9] by redirecting the stress and crack propagation. The challenge for tri-layer electrolytes is the gradual decay of capability for redirecting the stress and crack during long charge/discharge cycles. Cryogenic electron microscopy demonstrated that mechanically engineered transverse defects can redirect Li propagation away from the through-thickness direction, providing a new strategy for controlling Li penetration in SE.[10] A shape-memory alloy (SMA) coating was introduced onto $Li_7La_3Zr_2O_{12}$ to impose in-plane biaxial compressive stress, deflecting Li propagation into pathways parallel to the electrode/electrolyte interface. This work demonstrates the potential of stress engineering for regulating crack propagation through externally imposed compressive stress.[11] Nonetheless, imposing in-plane biaxial compressive stress in practical solid-state cells remains challenging. Therefore, it is highly desirable to develop a practical strategy capable of redirecting stress and crack propagation parallel to the electrode/electrolyte interface during prolonged cycles. However, such a strategy has yet to be realized.

Here we report an in situ self-organized lamellar multilayer that continuously redirects Li-bearing cracks parallel to the electrode under stack pressure. This lamellar multilayer forms in situ through sequential lithiation of an $Ag_{30}Sb_{70}$ precursor, where persistent mismatch strains generated between Li_2AgSb- and Li_3Sb-rich domains drive the spontaneous formation of alternating lamellae during cycling. Remarkably, rather than producing the through-thickness cracks normally favored by stack pressure, the mismatch strain continuously generates and regenerates densely stacked lamellae parallel to the electrode, establishing anisotropic pathways that guide Li-bearing cracks laterally throughout repeated Li plating and stripping. Unlike conventional artificial interlayers that decay in function with charge/discharge cycles, the lamellar architecture forms in situ, continuously evolves with electrochemical cycling, and develops into a multilayer framework instead of only a few discrete layers. Synchrotron X-ray fluorescence and electron microscopy reveal the formation and persistence of the lamellae; X-ray computed tomography shows lateral crack propagation within the lamellar framework; and coupled phase-field and finite-element simulations indicate that phase boundaries deflect through-thickness cracks into lateral pathways while maintaining Li in electronically connected regions. As a result, Li penetration is redirected along the pellet plane before reaching the SE. Li|$Ag_{30}Sb_{70}$||SE||$Ag_{30}Sb_{70}$|Li symmetric cells sustain

stepwise plating/stripping up to 9.0 mA cm^{-2} at 9.0 mAh cm^{-2}, and Li metal all-solid-state Li sulfur batteries (ASSLSBs) deliver 5.39 mAh cm^{-2} at 0.05 C. This in situ self-organized multilayer interfaces strategy establishes a cycling-adaptive route to Li-metal protection by governing crack direction rather than relying only on chemical passivation or mechanical blocking.

Lattice-mismatch-driven formation of lamellar architecture

The idea is inspired by stress-assisted microstructural evolution in multiphase metals, where lattice mismatch and mechanical contrast between adjacent phases drive directional structural evolution under external loading.[12] Since all-solid-state batteries operate under stack pressure, we hypothesized that electrochemical alloying could drive stress-assisted self-organization. Based on this concept, Ag-Sb alloys as a reactive two-phase precursor were prepared through one-step ball milling Ag and Sb powders with various molar ratios. Among them, $Ag_{30}Sb_{70}$ shows the highest critical current density (CCD, Supplementary Fig. 1) and was therefore used as a model alloy to investigate the structural evolution during battery operation.

$Ag_{30}Sb_{70}$ consists of orthorhombic ε (Ag_3Sb) and rhombohedral (Sb) phases at room temperature, as confirmed by the phase diagram and X-ray diffraction (XRD) analysis (Supplementary Figs. 2 and 3).[13]. Before ball milling, Ag and Sb powders exhibit nano- and microscale particle morphologies, respectively (Supplementary Fig. 4). After ball milling, irregularly shaped $Ag_{30}Sb_{70}$ particles are obtained, with Ag and Sb uniformly distributed throughout the particles, as confirmed by scanning electron microscopy (SEM) and energy-dispersive spectroscopy (EDS) mapping (Supplementary Fig. 5). The $Ag_{30}Sb_{70}$ powders were then pressed into pellets inside an argon-filled glovebox. Cross-sectional SEM images reveal nanoscale voids within the compacted structure (Supplementary Fig. 6A), while EDS mapping confirms that the homogeneous distribution of Ag and Sb is retained after pressing (Supplementary Fig. 6B-D). These observations indicate that the $Ag_{30}Sb_{70}$ precursor retains a homogeneous two-phase structure prior to electrochemical cycling.

Li|$Ag_{30}Sb_{70}$||SE||$Ag_{30}Sb_{70}$|Li symmetric cells were assembled to investigate the structural evolution of the $Ag_{30}Sb_{70}$ interlayer during electrochemical cycling. Synchrotron X-ray fluorescence (XRF) mapping was performed on cross-sections of the $Ag_{30}Sb_{70}$ interlayer before cycling (Fig. 1A) and after cycling (Fig. 1B). Before cycling, Ag and Sb remain uniformly distributed, consistent with the individual $Ag_{30}Sb_{70}$ pellets. After cycling, however, a pronounced

lamellar architecture develops throughout the $Ag_{30}Sb_{70}$ interlayer, confirming the spontaneous formation of an in situ self-organized lamellar interface.

Uniform Ag and Sb distributions are observed on the surfaces of both samples (Supplementary Fig. 7). Then, cross sections of both samples were further examined by SEM (Fig. 1C, D), which confirms the formation of the lamellar architecture after cycling (Fig. 1D). At the initial stage, Li_2AgSb and Li_3Sb phases are already detected under the combined effects of stack pressure and temperature (Supplementary Fig. 8A),[14,15], yet no lamellar architecture is observed (Fig. 1A, C). Upon subsequent electrochemical cycling (Supplementary Fig. 8B), distinct Li_2AgSb and Li_3Sb lamellar interfaces emerge, accompanied by alternating Ag-rich and Sb-rich domains (Fig. 1B, D). These observations indicate that Li incorporation proceeds through phase-dependent alloying rather than uniform lithiation, while the mechanism driving the self-organization of the lamellar architecture is explored below.

Here, we hypothesize that the lamellar architecture arises from the misfit strain between the Ag-rich and Sb-rich phases during cycling. Initially, Ag_3Sb and Sb coexist as a homogeneous two-phase precursor. During contact with Li and subsequent plating/stripping, the two phases lithiate sequentially: Sb-rich domains alloy with Li at a higher potential (~0.8 V) to form Li_3Sb-rich regions, whereas Ag-containing domains lithiate at a much lower potential (~0.07 V) to form Li_2AgSb-rich regions. This asynchronous alloying generates differential volume expansion and lattice-mismatch strain between adjacent phases. Under stack pressure, the accumulated strain is preferentially released through interfacial sliding and directional phase rearrangement, driving the spontaneous formation of an aligned lamellar architecture. Compared with a random two-phase morphology, the lamellar configuration more effectively accommodates differential lithiation strain and minimizes the overall strain energy. The lamellar architecture is continuously regenerated during electrochemical cycling, allowing local structural damage to be repeatedly repaired, unlike conventional prefabricated multilayers. The uniqueness of this in situ-formed aligned lamellar is that it will be shell-healed even if Li dendrites grow across the interface, which is impossible for all reported strategies.

To test our hypothesis, we performed a phase-field simulation (Details of the simulation can be found in the Methods). Three representative states were simulated to capture the microstructural evolution of the $Ag_{30}Sb_{70}$ system (Fig. 1E–G). Without external stack pressure, the system evolves into a random mixture of Ag-rich and Sb-rich phases (Fig. 1E), consistent with the morphology of

the as-prepared powders (Supplementary Fig. 5). Introducing stack pressure together with a small lattice-mismatch strain, corresponding to the initial stage before electrochemical cycling, results in only a weak tendency toward phase alignment, while the microstructure remains largely disordered (Fig. 1F), in agreement with the experimental observations (Fig. 1A, C). In contrast, when a larger lattice-mismatch strain associated with substantial Li incorporation is introduced under the same stack pressure, the microstructure spontaneously evolves into a vertically aligned lamellar architecture composed of alternating Ag-rich and Sb-rich phases (Fig. 1G), consistent with the cycled samples (Fig. 1B, D). These simulations demonstrate that stack pressure alone is insufficient to generate the lamellar architecture, instead, substantial lattice-mismatch strain generated during electrochemical alloying, together with stack pressure, drives its spontaneous self-organization.

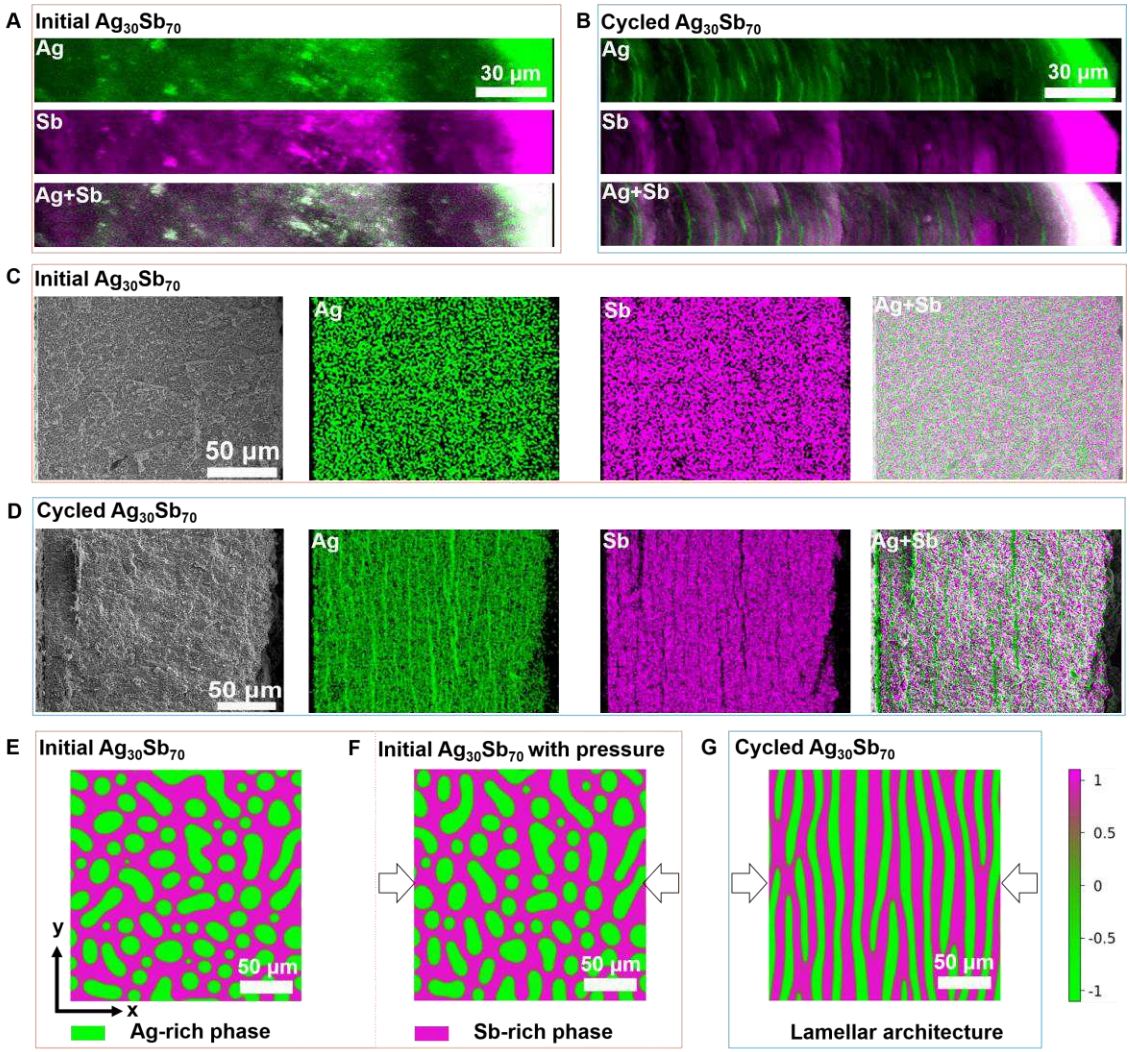


Fig. 1 | Formation of lamellar architecture in $Ag_{30}Sb_{70}$ during electrochemical cycling. **A, B,** XRF elemental mappings. **C, D,** SEM image and EDS elemental mappings. **E-G,** Simulation results of Li containing $Ag_{30}Sb_{70}$ layer consisting two-phase mixture of Ag-rich (green) and Sb-rich (magenta). (**E**) Without external pressure and without considering Li-induced volume strain. (**F**) With external pressure and considering small Li-induced volume strain. (**G**) With external pressure and considering large Li-induced volume strain.

Li metal anode stabilization through Lamellar architecture

The impact of $Ag_{30}Sb_{70}$ on the Li stripping/plating behavior was more systemically investigated using Li||SE||Li and Li|$Ag_{30}Sb_{70}$||SE||$Ag_{30}Sb_{70}$|Li symmetric cells. Li||SE||Li symmetric cells present CCDs of 0.4 mA cm^{-2}/0.4 mAh cm^{-2} at 25 °C, 1.2 mA cm^{-2}/1.2 mAh cm^{-2} at 60 °C, and 1.8 mA cm^{-2}/1.8 mAh cm^{-2} at 80 °C (Fig. 2A), consistent with previous reported values.[16] In contrast, incorporating the $Ag_{30}Sb_{70}$ interlayer markedly improved the performance. Li|$Ag_{30}Sb_{70}$||SE||$Ag_{30}Sb_{70}$|Li symmetric cells operated without short circuit up to 2.4, 7.6, and 9.0 mA cm^{-2} (with matched areal capacities) at 25, 60, and 80 °C, respectively (Fig. 2B-D). The obtained evaluations exhibit noticeable improvements compared with previously reported results.[16] By contrast, control cells with single-phase interlayers exhibited substantially higher polarization (Supplementary Fig. 1A, H), highlighting the importance of the in situ formed lamellar architecture in simultaneously stabilizing the Li/SE interface and facilitating Li-ion transport. To further evaluate long-term stability, Li|$Ag_{30}Sb_{70}$||SE||$Ag_{30}Sb_{70}$|Li symmetric cells were first cycled under stepwise increasing current densities to 6.0 mA cm^{-2} within the initial 30 cycles and subsequently operated at 6.0 mA cm^{-2}/6.0 mAh cm^{-2} for 500 cycles. The stable cycling behavior confirms that the lamellar architecture effectively suppresses dendrite propagation while maintaining robust interfacial compatibility with both the Li metal anode and the SE.

Moreover, Supplementary Fig. 9 directly compares the morphology of the cycled SE without and with the $Ag_{30}Sb_{70}$ interlayer. In the absence of $Ag_{30}Sb_{70}$, metallic Li remained tightly embedded within the SE, making the interface difficult to separate (Supplementary Fig. 9A), indicating severe Li penetration into the electrolyte during repeated stripping/plating. Such mechanical interlocking is closely associated with dendrite propagation and eventual short-circuit failure. In contrast, the SE could be readily detached after cycling with $Ag_{30}Sb_{70}$, leaving a smooth and intact surface (Supplementary Fig. 9B). This contrast indicates that the in situ generated lamellar architecture

transforms the interface from mechanically locked to mechanically compliant, mitigating Li penetration and improving interfacial compatibility. The mechanism by which this lamellar architecture suppresses Li dendrite growth is discussed in the following section.

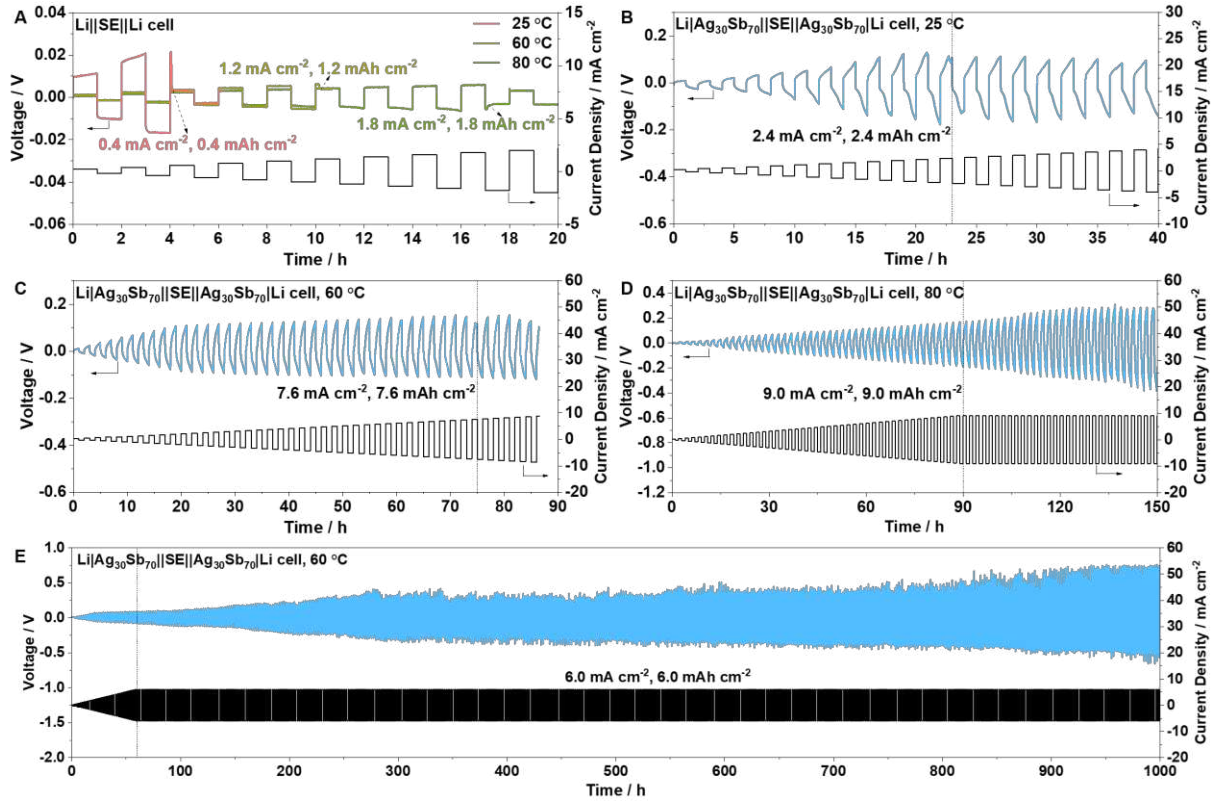


Fig. 2 | Enhanced electrochemical performance enabled by $Ag_{30}Sb_{70}$ in symmetric Li cells. **A-D,** Voltage profiles of symmetric cells under stepwise increasing current densities and corresponding capacities, with a constant Li stripping/plating time of 1 h. **A,** Voltage profiles of Li||SE||Li cell at 25, 60 and 80 °C. Voltage profiles of Li|$Ag_{30}Sb_{70}$||SE||$Ag_{30}Sb_{70}$|Li cell at 25 (**B**), 60 (**C**), and 80 °C (**D**). **E,** Voltage profiles of Li|$Ag_{30}Sb_{70}$||SE||$Ag_{30}Sb_{70}$|Li cell at 60 °C with stepwise increasing current densities and capacities to 6 mA cm^{-2}/6 mAh cm^{-2} and then galvanostatically stripping/plating in the following cycles.

Mechanism of dendrite suppression via self-organized lamellar interfaces

The improved CCDs originate from the effective suppression of Li dendrite growth. We first examined whether the lamellar architecture could be maintained during prolonged cycling. As shown in Fig. 3A, Supplementary Fig. 10 and 11, the lamellar architecture remains well preserved

after 5, 10, and 100 cycles. Importantly, lamellar morphology is maintained during both the Li plating and stripping processes, demonstrating robust structural stability under repeated electrochemical cycling. This persistent structure originates from the sequential lithiation behavior of the Ag-rich and Sb-rich phases. Their distinct alloying potentials and lithiation kinetics continuously regenerate lattice-mismatch strain across the interfaces, enabling the lamellar architecture to self-organize and maintain structural integrity under repeated electro-chemo-mechanical cycling.

The stable lamellar architecture provides the structural basis for regulating Li dendrite growth by introducing spatial heterogeneity in mechanical properties and interfacial energetics.[17–19] During Li deposition, such heterogeneity induces nonuniform stress and deposition distribution near the Li interface, promoting localized deformation and crack initiation within the structure. X-ray computed tomography (XCT) further reveals pronounced lateral crack propagation within the $Ag_{30}Sb_{70}$ framework (Fig. 3B), indicating that crack propagation is redirected along the lamellar phase interfaces rather than penetrating directly through the whole structure. This behavior agrees with previous predictions that mechanically weak interfaces can redirect Li dendrite propagation and suppress dendrite-induced short circuits.[10] Here, this concept is experimentally realized through an in-situ formed self-organized lamellar architecture that is continuously regenerated during cycling. In addition, the electronically conductive framework enables the electrochemical stripping of trapped or isolated Li within the lamellar structure, facilitating dead Li reutilization. Together, these features continuously regulate dendrite propagation and maintain stable cycling.

The mechanism of crack redirection was further investigated using a coupled phase-field and finite-element modeling framework (Supplementary Fig. 12). The simulations were performed on a half-cell configuration consisting of a Li metal anode and the Ag-Sb structure. Li deposition under nonuniform interfacial contact was first simulated using a phase-field model (Supplementary Fig. 13), and the resulting deposition profile was subsequently incorporated into a finite-element model to simulate crack propagation during continued Li growth (Fig. 3C, and D). In the absence of lamellar architecture, cracks propagate continuously through the structure without deflection (Fig. 3C). In contrast, in the presence of the lamellar architecture, cracks initially propagate perpendicular to the Li surface but are redirected along the Ag-rich/Sb-rich interfaces once they reach the phase boundaries (Fig. 3D). This behavior originates from the pronounced fracture-toughness mismatch between the two phases and is consistent with the established crack-deflection

criterion for bi-material systems (Supplementary Fig. 14).[20,21] In the present system, both the fracture-toughness ratio ($\frac{\Gamma_i}{\Gamma_m}$ =0.0005) and the cohesive-strength ratio ($\frac{\hat{\sigma}_i}{\hat{\sigma}_m} = 0.073$) satisfy the conditions for crack deflection, leading to preferential crack propagation along the Ag-rich/Sb-rich interfaces (Fig. 3D). Additional modeling details are provided in the Methods.

Li deposition within cracks was further investigated using a phase-field model coupled with electrochemical reactions and mechanical stress. The crack geometry obtained from finite-element modeling was imported into the phase-field simulation to capture Li plating behavior. The results reveal a reciprocal coupling between Li dendrite growth and crack propagation. High curvature at the crack surfaces and crack tips concentrates the local current density (Supplementary Fig. 15), promoting preferential Li deposition along the crack pathways, which reduces Li^+ into Li and deposited therein. This drives Li dendrite growth along the crack pathways (Fig. 3E, and F). The deposited Li subsequently generates localized stress concentrations near the crack tip. The first principal stress, which governs crack initiation and propagation, is highly concentrated at the crack tip (Supplementary Fig. 16A), with its direction dictating the propagation trajectory. Meanwhile, the Tresca stress, representing the maximum shear stress, is also localized in this region (Supplementary Fig. 16B). The coexistence of elevated normal and shear stresses at the crack tip governs mixed-mode crack propagation. In the presence of the self-organized lamellar architecture, crack propagation is repeatedly redirected along the Ag-rich/Sb-rich interfaces, interrupting continuous dendrite growth pathways and preventing penetration toward the SE. By contrast, without the lamellar architecture, cracks propagate continuously through the structure, enabling Li dendrites to penetrate the SE and eventually induce short-circuit failure.

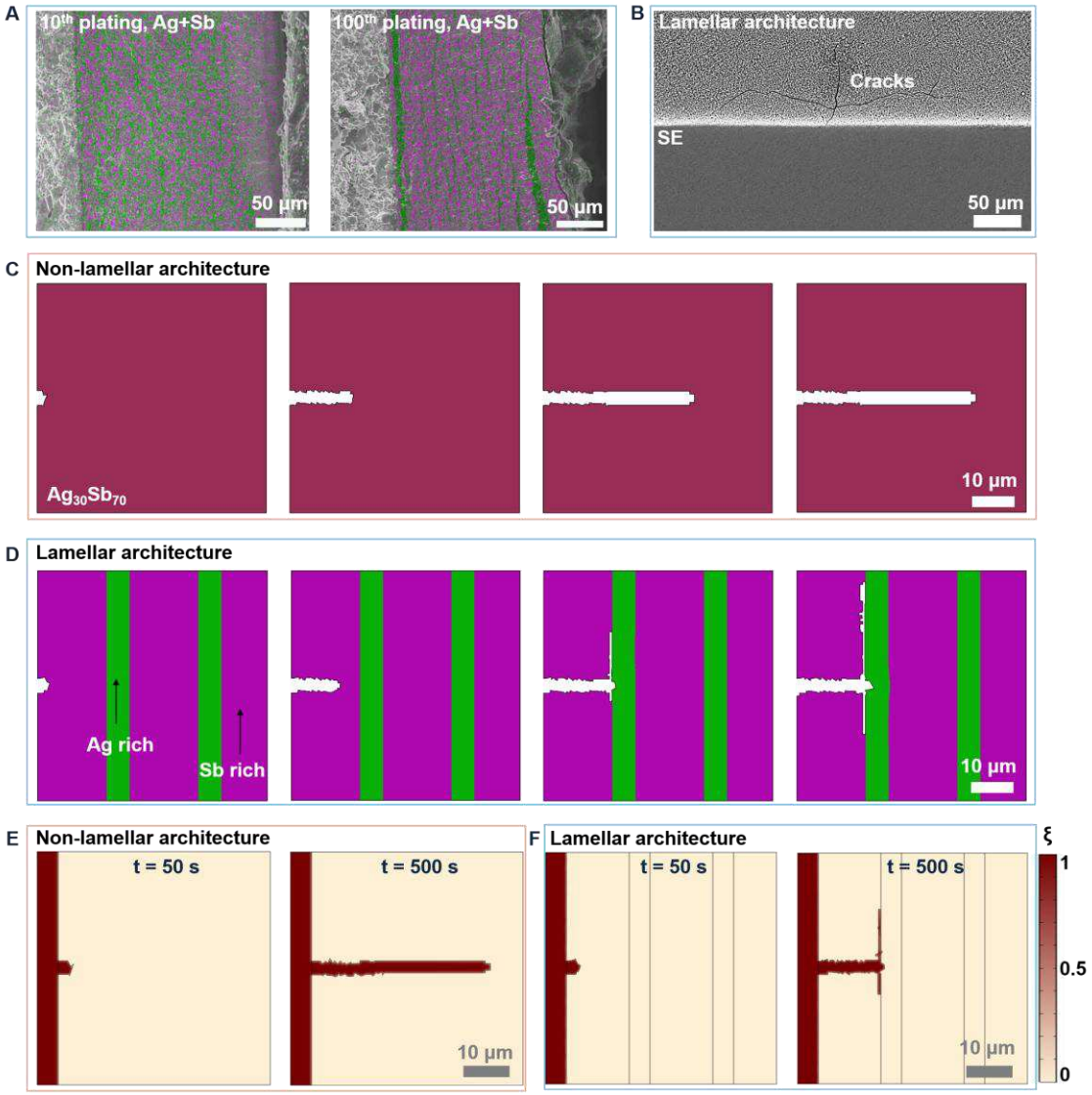


Fig. 3 | Suppression of Li dendrite propagation by the lamellar interfaces. A, EDX elemental mapping of Ag (green) and Sb (magenta) after 10 and 100 cycles. **B,** XCT visualization of crack distribution. **C, D,** Finite element modelling result showing crack propagation in the non-lamellar architecture (**C**) and lamellar structure (**D**). **E, F,** Phase-field simulations showing the evolution of the Li metal in the non-lamellar architecture (**E**) and lamellar architecture (**F**).

Electrochemical performance of all-solid-state Li-sulfur batteries (ASSLSBs)

The electrochemical performance of the in situ generated self-organized lamellar architecture was further evaluated in ASSLSBs consisting of a Li metal anode, a SE, and a sulfur (S) cathode (30 wt.%, Supplementary Fig. 17). Electrochemical impedance spectroscopy (EIS) and distribution of

relaxation time (DRT) analyses reveal that introducing the $Ag_{30}Sb_{70}$ interlayer only slightly increases the bulk and charge-transfer resistances, while the overall cell polarization remains essentially unchanged before short-circuit failure of the Li||SE||S cell (Fig. 4A-C and Supplementary Fig. 18). This result indicates that the additional interfacial resistance is not rate-limiting. Instead, the self-generated lamellar architecture effectively homogenizes Li deposition and suppresses localized polarization. Consistent with these observations, Li|$Ag_{30}Sb_{70}$||SE||S cells exhibit excellent rate capability over 0.05-0.5 C with a sulfur mass loading of 3.0 mg cm^{-2} at 60 °C (Fig. 4D-F and Supplementary Fig. 19), delivering areal capacities of 5.39, 4.59, 3.09, and 1.79 mAh cm^{-2} at 0.05, 0.1, 0.2, and 0.5 C, respectively. When the rate returns to 0.05 C, the capacity recovers to 5.17 mAh cm^{-2}, indicating good reversibility. These results demonstrate that the in-situ generated self-organized lamellar architecture enables fast Li-ion transport while maintaining stable interfacial compatibility in ASSLSBs.

Then, the cyclic stability of ASSLSBs was evaluated over a wide range of operating conditions. with sulfur mass loadings of 1.0 and 3.0 mg cm^{-2} at 0.1 C under 25 °C (Fig. 4G, Supplementary Fig. 20 and 21). Li|$Ag_{30}Sb_{70}$||SE||S cells deliver an initial areal capacity of 1.40 and 4.18 mAh cm^{-2}, and maintain 0.89 and 2.16 mAh cm^{-2} after 100 cycles, respectively. Stable cycling was further achieved at elevated temperature. At 60 °C and 0.5 C, Li|$Ag_{30}Sb_{70}$||SE||S cell delivered an initial areal capacity of 1.75 mAh cm^{-2} and retained approximately 70% of its capacity after 250 cycles (Fig. 4H and Supplementary Fig. 22). Moreover, Li|$Ag_{30}Sb_{70}$||SE||S cell was investigated at 0.15 C and 60 °C with an areal S loading of 3.0 mg cm^{-2} (Fig. 4I and Supplementary Fig. 23). The cell displayed an initial areal capacity of 4.91 mAh cm^{-2} and maintained around 70% capacity retention after 100 cycles. In contrast, the Li||SE||S cell employing bare Li anode suffered short-circuit failure during the initial charging cycle at sulfur mass loadings of 1.0 and 3.0 mg cm^{-2}(Supplementary Fig. 24), consistent with previous reports.[16] In contrast to prior studies that predominantly rely on Li-In anodes (Supplementary Table 1), the in-situ generated self-organized lamellar architecture enables stable long-term cycling using Li metal.

Additionally, ASSLSBs delivered capacities exceeding the theoretical capacity of sulfur, irrespective of the presence of $Ag_{30}Sb_{70}$. To identify the origin of this excess capacity, Li-In||SE||KB/S/LGPS (Supplementary Fig. 25) and Li|$Ag_{30}Sb_{70}$||SE||KB/LGPS (Supplementary Fig. 26) cells were assembled as control systems. The results indicate that the excess capacity originates from the catholyte LGPS, which undergoes reversible redox reactions during battery operation.

Specifically, LGPS contributes up to ~240 mAh g^{-1} of reversible capacity (Supplementary Fig. 26), thereby enhancing the overall discharge performance.

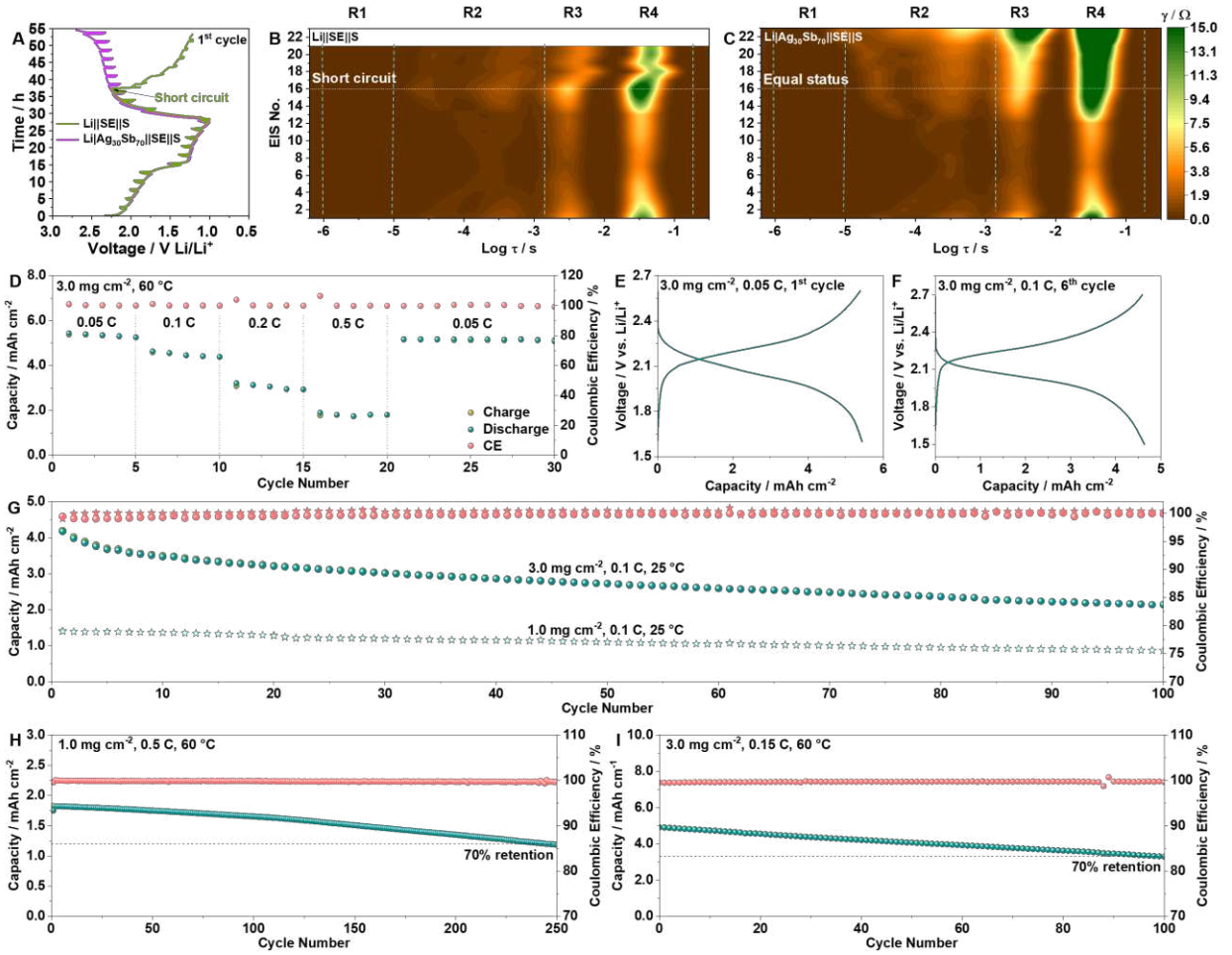


Fig. 4 | Electrochemical performance of ASSLSBs. **A,** Dis-/charge profiles, and **B, C,** two-dimensional color mappings of the DRT curves of Li||SE||S and Li|$Ag_{30}Sb_{70}$||SE||S cell. **D-I,** Electrochemical performance of Li|$Ag_{30}Sb_{70}$||SE||S cell. (**D**) The C-rate capability from 0.05 C to 0.5 C under 60 °C, and corresponding (**E, F**) dis-/charge profiles at 0.05 and 0.1 C. (**G-I**) Dis-/charge specific capacity and coulombic efficiency at (**G**) 0.1 C and 25 °C, (**H**) 0.5 C and 60 °C, (**I**) 0.15 C and 60 °C. The sulfur mass loadings are (**G, H**) 1.0 mg cm^{-2} and (**D, G, I**) 3.0 mg cm^{-2}. The lamellar architecture remains robust even when its thickness is reduced by half (Supplementary Fig. 8, 9).

A substantially thinner $Ag_{30}Sb_{70}$ interlayer was further investigated (Supplementary Fig. 27). Despite the reduced thickness, the characteristic lamellar architecture was still generated during electrochemical cycling, suggesting that the self-organization process is not restricted to the thick model interlayer employed in this work. These observations further support the potential of the in situ generated lamellar architecture as an interfacial design concept for stabilizing lithium metal anodes.

Conclusions

By converting lithiation-induced lattice mismatch into an in situ self-organized lamellar architecture that programs crack trajectories, the Ag-Sb interface establishes a dynamic route for stabilizing Li metal in sulfide-based all-solid-state Li-S batteries. During cycling, sequential lithiation of Ag-rich and Sb-rich regions generates alternating Li_2AgSb- and Li_3Sb-rich domains whose strain mismatch and mechanical contrast continuously drive the formation and maintenance of Ag-rich/Sb-rich lamellae under stack pressure. Rather than functioning as a passive interfacial barrier, the self-organized lamellar architecture evolves together with electrochemical cycling, accommodates repeated electro-chemo-mechanical deformation, redirects Li-bearing cracks parallel to the electrode, and preserves electrochemical access to confined Li before through-thickness penetration occurs. As a result, Li failure is mitigated not by attempting to create a permanently crack-free or mechanically impenetrable barrier, but by controlling where cracks propagate and whether Li deposited in those pathways remains electrochemically recoverable. This work extends the emerging view that dendrite short-circuiting in solid-state batteries is governed by crack initiation and propagation, and advances it by demonstrating that crack trajectories can be dynamically programmed through in situ interfacial self-organization. More broadly, mismatch-interface engineering offers a design principle for high-energy solid-state batteries in which interfacial strain, traditionally viewed as a source of degradation, is harnessed as a driving force for adaptive protection, self-organization and dendrite redirection.

Methodes

Materials

Lithium sulfide (Li_2S, 99.98%), phosphorus pentasulfide (P_2S_5, 99%), lithium chloride (LiCl, >99.98%), sulfur (99.98%), silver powder (Ag, <100 nm, 99.5% trace metal basis), and

antimony powder (Sb, 100 mesh, 99.5% trace metal basis) were purchased from Sigma-Aldrich. Germanium (IV) disulfide powder (>99.99%, 325 Mesh) was purchased from MSE supplies.

Synthesis of the electrolyte $Li_{5.4}PS_{4.4}Cl_{1.6}$ and catholyte $Li_{10}GeP_2S_{12}$

The sulfide solid electrolyte (SE) $Li_{5.4}PS_{4.4}Cl_{1.6}$ was synthesized via a conventional ball milling and annealing process. Specifically, 1.310 g of Li_2S, 1.665 g of P_2S_5, and 1.017 g of LiCl were mixed in a stainless-steel jar under an argon atmosphere. Ball milling was carried out at 500 rpm for 40 cycles, with each cycle consisting of 15 minutes of milling followed by a 15-minute rest. The weight ratio of ZrO_2 balls to the precursor mixture was 50:1. After milling, the mixture was sealed in a glass tube and annealed at 510 °C for 2 hours, yielding the $Li_{5.4}PS_{4.4}Cl_{1.6}$ electrolyte.

For $Li_{10}GeP_2S_{12}$, 1.5608 g of Li_2S, 1.5101 g of P_2S_5, and 0.9292 g of GeS_2 were mixed in a stainless-steel jar. Subsequently, ball milling was performed at a speed of 380 rpm for 20 hours. The obtained powder was then compressed under a pressure of 120 MPa to form pellet. Next, 0.5 g pellet was sealed in a glass tube and annealed at 550 °C for 24 hours.

Synthesis of the Ag_xSb_y

Sb and Ag powder with various molar ratio were mixed in a stainless-steel jar under an argon atmosphere. Ball milling was carried out at 500 rpm for 40 cycles, with each cycle consisting of 15 minutes of milling followed by a 15-minute rest. Then, the resulting product was collected for future use.

Preparation of sulfur cathodes

The cathode materials were prepared via mixing catholyte ($Li_{10}GeP_2S_{12}$), S and ketjenblack with weight ratios of 20:30:50 through ball milling and melting-infiltration methods. The mixture together with ZrO_2 balls in a weight ratio of 1:20 was sealed in a stainless-steel jar under a protective argon atmosphere and milled at 400 rpm for 10 h. Subsequently, the mixture is sealed within a glass tube and heated at 155 °C for 12 h. The resulting product was collected as the cathode material.

Electrochemical characterization

All cells are assembled inside the Ar-filled glovebox ($O_2 < 0.1$ ppm, $H_2O < 0.1$ ppm). For Li||SE||Li symmetric cell, 150 mg SE powders were pressed under 400 MPa to form a pellet with a diameter of 12.8 mm. Then, a piece of Li foil and copper current collector were attached. For $Li|Ag_xSb_y||SE||Ag_xSb_y|Li$ symmetric cell, Ag_xSb_y was uniformly spread onto both sides, after which a piece of Li foil and copper current collector were attached. The cells were tested under 20

MPa.

In full-cell preparation, 150 mg SE powders were pressed under 40 MPa to form a pellet. Then, sulfur cathode material was uniformly spread onto one side, after which an aluminum current collector was placed on top. The assembly was pressed under a pressure of 400 MPa for 3-5 minutes. For Li||SE||S cell, a piece of Li foil and copper current collector were attached. For $Li|Ag_xSb_y||SE||S$ cell, Ag_xSb_y was uniformly spread onto the opposite side, after which a piece of Li foil and copper current collector were attached. The cells were tested under 20 MPa. The sulfur content is 30%. The mass loadings of sulfur were 1.0, 3.0 and 4.5 mg cm^{-2}.

Symmetric cells and Li sulfur cells were evaluated via an electrochemical station (Bio-Logic SP-150). Electrochemical impedance spectroscopy (EIS) was carried out with an amplitude of 10 mV over a frequency range of 1 MHz to 0.1 Hz. The distribution of relaxation time (DRT) was analyzed based on EIS results using Bayesian calculations in MATLAB.

Material characterization

Scanning electron microscopy (SEM), energy-dispersive X-ray spectroscopy (EDS) and X-ray diffraction (XRD). SEM morphologies and EDS analyses were obtained on a Hitachi S4800 scanning electron microscope operated at an accelerating voltage of 3 kV. XRD measurements were performed using Cu Kα radiation over a 2θ range of 10-90°. For samples extracted from the cells, a layer of Kapton tape was applied to the surface during measurement to protect them from oxidation.

Synchrotron X-ray characterization (XRF). XRF mapping was performed at the 2-ID-D beamline at the Advanced Photon Source, Argonne National Laboratory. 12.0 keV X-ray photons were selected and focused onto the sample to 300 nm spot size. The pre-cycled samples were mounted on the holder and the interface was aligned to be perpendicular to the X-ray propagation direction. XRF signals were collected by the single-element energy-dispersive Vortex detector. The samples were raster-scanned with 300nm step size across the interface to measure the element distribution. The data was then processed and quantified by XRF_MAPS software.

X-ray computed tomography (XCT). The $Li|Ag_xSb_y||SE||Ag_xSb_y|Li$ cell was constructed in a PEEK tube with an inner diameter of 2 mm. Approximately 4 mg of SE powder was loaded and compressed using two stainless steel rods to form a dense pellet. Ag_xSb_γ powders were uniformly applied to both sides of the SE pellet, followed by the attachment of Li metal and copper current collectors. The stainless steel rods were fixed to the PEEK tube via a screw connection, enabling

the application of external stacking pressure during testing.

The XCT scans were collected at the Oak Ridge National Laboratory using a Zeiss Xradia Versa 520 system operated at 60 kV and 5W. A 20x scintillator objective was used for increased resolution coupled with a 2 × 2 binning on the detector side for improved counts. With this setup, a voxel size of 0.702 μm was achieved. The XCT data were collected over a full 360° rotation of the sample (around the vertical axis) with 1601 evenly spaced projections. Raw data was reconstructed with the Zeiss reconstructor software and .tiff stacks were obtained for further processing. Image segmentation and 3D rendering creation were performed using DragonFly.

Phase-field simulations

Formation of lamellar architecture in $Ag_{30}Sb_{70}$

To simulate the microstructural evolution associated with two-phase separation in the $Ag_{30}Sb_{70}$ system, phase-field modeling was employed. A composition order parameter (c = -1.0 ~ 1.0) was used to distinguish the Ag-rich phase (green, c = -1) and the Sb-rich phase (magenta, c = 1). The total free energy of the system consists of bulk chemical energy, interfacial gradient energy, and mechanical strain energy, all expressed as functions of c. The morphological evolution of the two-phase system, described by c(r), is driven by the Cahn–Hilliard equation,

$$\frac{\partial c}{\partial t} = \nabla \bullet \left(M \nabla \frac{\delta F}{\delta c} \right) \quad (1)$$

where M is the mobility and F is total free energy of the system. The latter is written as,

$$F = \int_V [f_{chem}(c) + f_{grad}(\nabla c) + E_{el}]\, dV \quad (2)$$

where $f_{chem}(c)$is the bulk chemical energy density, $f_{grad}(\nabla c)$ is the gradient energy density, and E_{el} is the elastic strain energy density, respectively. The bulk chemical energy density describes the thermodynamic equilibrium of the system. It is written as $f_{chem}(c) = -\frac{1}{2}c^2 + \frac{1}{4}c^4$ which yields two local minimum at $c(r) = 1$ and $c(r) = -1$, corresponding to the Sb-rich phase and Ag-rich phase. The gradient energy density describes the energy associated with the interface between the Ag-rich and Sb-rich phases. In the diffuse-interface model, it is represented by the gradient of the order parameter $c(r)$, i.e., $f_{grad}(\nabla c) = \frac{1}{2}\kappa(\nabla c)^2$ in which κ is the gradient energy coefficient.

The elastic strain energy density of a two-phase system with inhomogeneous elastic moduli is,

$$E_{el} = \frac{1}{2} C_{ijkl}(r) \varepsilon_{ij}^{el} \varepsilon_{kl}^{el} \quad (3)$$

where $C_{ijkl}(r)$ is the local elastic modulus and is represented by the composition field as $C_{ijkl}(r) = C^0_{ijkl} + C^1_{ijkl}\delta c(r)$, where C^0_{ijkl} is the average modulus of the system, C^1_{ijkl} is a constant proportional to the elastic moduli difference between the two phases, and $\delta c(r)$ is local composition variation in the system and is written as $\delta c(r) = c(r) - c_0$ where c_0 is the average composition of the reference state. In an inhomogeneous system, the local elastic strain $\varepsilon^{el}_{kl}(r)$ (as in Eq. (3)) is calculated to be the difference between the homogeneous strain $\overline{\varepsilon_{kl}}$, local heterogeneous strain $\delta\varepsilon_{kl}(r)$, the a local stress-free strain $\varepsilon^0_{kl}(r)$, i.e.,

$$\varepsilon^{el}_{kl}(r) = \overline{\varepsilon_{kl}} + \delta\varepsilon_{kl}(r) - \varepsilon^0_{kl}(r) \quad (4)$$

The homogeneous strain $\overline{\varepsilon_{kl}}$ determines the macroscope volume change induced by externally applied pressure. The local heterogeneous strain $\delta\varepsilon_{kl}(r)$ describes the local displacement and satisfies $\int_V \delta\varepsilon_{kl}(r)\, dV = 0$. The local stress-free strain $\varepsilon^0_{kl}(r)$ characterizes the local inhomogeneity induced by the local composition variation $\delta c(r)$. $\varepsilon^0_{kl}(r)$ is usually calculated based on the Vegard's law,

$$\varepsilon^0_{kl}(r) = \varepsilon_0 \delta c(r) \delta_{kl} \quad (5)$$

where ε_0 is the composition expansion coefficient, also known as the Vegard's coefficient. δ_{kl} is the Kronecker-delta function. Finally, the local elastic stress $\sigma_{ij}(r)$is related to the elastic strain $\varepsilon^{el}_{kl}(r)$ based on Hooke's law, i.e., $\sigma_{ij}(r) = C_{ijkl}(r)\varepsilon^{el}_{kl}(r)$. The elastic stress $\sigma_{ij}(r)$ needs to satisfy the mechanical equilibrium condition, i.e., $\partial\sigma_{ij}/\partial x_j = 0$.

Initially, the $Ag_{30}Sb_{70}$ system is in a homogeneous state with uniform distribution of composition field variable (c_0 = 0.2). Random noise is then added onto c_0 to enable the system to evolve into mixed Ag-rich and Sb-rich phases, represented by the two local minima (c = -1 and c = 1) of the chemical free energy function ($f_{chem}(c)$). We chose c_0 = 0.2 to yield the volume fractions of the Ag-rich (c = -1) and Sb-rich phase (c = 1) to be 40% and 60%, which is calculated from lever rule. The calculated volume fraction ratios of the two phases agree with the $Ag_{30}Sb_{70}$ alloy based on the phase diagram (Supplementary Fig. 2). The elastic constants for Ag-rich phase and Sb-rich phase are selected as (C_{11} = 63.62, C_{12} = 46.47, C_{44} = 56.12) and (C_{11} = 49.63, C_{12} = 36.96, C_{44} = 53.98) in the units of GPa, respectively, which are based on literature.[22,23] The homogenous strain due to applied external pressure along x-axis is set to be $\overline{\varepsilon_{11}}$ = -0.004. Additionally, the Vegard's strain coefficients are set to be ε_0 = 0.02 and ε_0 = 0.08 before and after electrochemical cycling, representing the local strain heterogeneity arising from Li incorporation.

Phase-field simulation of crack propagation and Li growth

To further understand the effect of $Ag_{30}Sb_{70}$ on the lithium plating and stripping process, we performed phase-field simulations coupled with solid mechanics and electrochemistry. A half-cell model consisting of a Li anode and an Ag–Sb structure is considered for the simulation. A phase-field order parameter ξ is introduced to represent Li anode (ξ = 1) and $Ag_{30}Sb_{70}$ region (ξ = 0). The total energy of the system is given by,

$$F = \int_V [f_{ch}(\xi, C_i) + f_{grad}(\nabla\xi) + f_{elec}(C_i, \varphi)]\, dV \qquad (6)$$

where f_{ch}, f_{grad}, and f_{elec} are the chemical free energy, gradient energy, and electrical energy, respectively. The local chemical free energy is expressed as $f_{ch} = W\xi^2(1-\xi)^2$, where W is the barrier height of the double well function. The gradient energy takes the form $f_{grad} = \frac{\kappa}{2}(\nabla\xi)^2$, where κ is the gradient energy coefficient. Anisotropic gradient energy coefficient is used for the Li anode to simulate dendrite growth, i.e., $\kappa = \kappa_0[1 + \delta\cos(w\theta)]$, where κ_0, δ, w, and θ are surface energy, strength of anisotropy, mode of anisotropy, and angle between the normal vector to the interface and the reference axis, respectively. Additional detailed information about these energies can be found in the references.[24,25]

The temporal evolution of Li anode during plating process is governed by the following equation,

$$\frac{\partial\xi}{\partial t} = -L_\xi\left\{\frac{\partial f_{ch}}{\partial\xi} - \kappa(\nabla^2\xi)\right\} - L_\eta h'(\xi)\left\{exp\left[\frac{\alpha zF\eta}{RT}\right] - C^*_{Li^+}\ exp\left[\frac{-(1-\alpha)zF\eta - zF\eta_m}{RT}\right]\right\} \qquad (7)$$

where, L_ξ and L_η are the lithium interface mobility and reaction constant, respectively. F is Faraday's constant, t is time, α is a symmetric factor, R is the gas constant, T is the temperature, z is the charge number, and η is overpotential. η_m is an additional potential term induced by mechanical stress, which modifies overpotential, and is expressed as $\eta_m = \frac{\sigma V_m}{F}$, where σ is mechanical stress and V_m is the molar volume. $h'(\xi)$ is the first derivative of the interpolation function $h(\xi) = \xi^3(10 - 15\xi + 6\xi^2)$.

The evolution of Li^+ concentration during the cycling process is governed by the equation,

$$\frac{\partial C^*_{Li^+}}{\partial t} = \nabla\cdot\left[D^{eff}\nabla C^*_{Li^+} + \mu_{Li}C^*_{Li^+}\, zF\nabla\phi\right] - K\frac{\partial\xi}{\partial t} \qquad (8)$$

Where D^{eff} is the effective diffusivity of Li^+ ions in the system. The system is divided into four different domains – Li metal, crack, Ag-rich phase and Sb-rich phase – and materials based properties such as Li^+ diffusivity, electrical conductivity and Young's modulus were assigned at

each domain. μ_{Li} is the mobility of Li^+ ions, and K is the accumulation/annihilation rate of Li^+ at the Li surface.

The electric potential distribution in the system is obtained by solving the current continuity equation,

$$\nabla \cdot (\sigma^{eff} \nabla \phi) = R_e \frac{\partial \xi}{\partial t} \quad (9)$$

where ϕ is the electrical potential and σ^{eff} is the effective electrical conductivity of the system. R_e is the current constant.

Finally, the mechanical equilibrium equation is solved to obtain local stress and strain distribution in the system and its effect on the cycling process.

$$\nabla \cdot \boldsymbol{\sigma} = 0 \quad (10)$$

where σ is the mechanical stress, which is written as $\sigma = C_{ijkl} * \varepsilon_{ij}^{el}$. The elastic strain ($\varepsilon_{ij}^{el}$) is calculated as $\varepsilon_{ij}^{el} = \varepsilon_{ij} - \varepsilon_{ij}^{0}$, where ε_{ij} is a total strain, ε_{ij}^{0} is Vegard's strain, and C_{ijkl} is a elastic stiffness tensor. The Young's modulus for the Li anode, Ag-rich phase and Sb-rich phase are assigned as 4.9 GPa, 24.42 GPa and 28.59 GPa, respectively.

Equations 7-10 were solved on the COMSOL Multiphysics software using the finite element method. The model geometry is chosen to be a square-shaped 2D domain having a side length of 50 μm. For the order parameter ξ, zero flux boundary conditions were applied, whereas for the electric potential (ϕ) and Li^+ concentration (C_{Li^+}) Dirichlet boundary conditions were applied. Electrical potential of ϕ = 0V and ϕ = -0.3 V were applied at right and left boundaries, respectively. Similarly, for the mechanical boundary conditions, $u_y = 0$ condition was applied at the top and bottom boundaries, $u_y = 0$ $u_x = 0$ condition was applied at right boundary, whereas stack pressure (20 MPa) was applied at the left boundary. All the parameters were normalized into unitless quantities using the characteristic time (t_0), characteristics length (l_0), and characteristics energy (E_0). Likewise, C_{Li^+} is normalized by dividing it with the bulk concentration of Li^+ ions, which is given by $C_{Li^+}^* = C_{Li^+}/C_0$, where C_0 = 9 mol L^{-1}. Regarding the Li^+ boundary condition, the vaule of $C_{Li^+}^*$ is set to be 1 at the right boundary.

Continuum damage modeling of the crack deflection and dendrite growth suppression mechanism

Continuum damage modeling has been performed to illustrate the mechanism governing the crack

deflection observed in material characterization. The continuum damage model is implemented through elastoplastic constitutive laws and cohesive damage models, leveraging the commercial finite element analysis (FEA) package Abaqus. The Young's moduli for the Li anode, Ag-rich phase, Sb-rich phase, and $Ag_{30}Sb_{70}$ are assigned as 4.9 GPa,[26] 24.42 GPa,[23] 28.59 GPa,[22] and 27.34 GPa. We were unable to find the modulus of $Ag_{30}Sb_{70}$ in literature and therefore applied the linear rule of mixture, mixing 30% of the Ag-rich phase modulus and 70% of the Sb-rich phase modulus. The yield strength and ultimate strength of the Ag-rich phase are 33.2 MPa and 155.7 MPa, taken as an average of pure Ag and pure Sb.[27–29] The yield strength of the Sb-rich phase is 11.4 MPa, taken from pure Sb.[29] Again, due to the lack of data in the literature, the yield strength of $Ag_{30}Sb_{70}$, 17.94 MPa, is calculated as a linear mixing of 30% of the Ag-rich phase yield strength and 70% of the Sb-rich phase yield strength. As the Sb-rich phase and $Ag_{30}Sb_{70}$ are brittle, the materials would undergo brittle failure immediately after yielding, so the concept of ultimate strength is not applicable. After the Ag-rich phase reaches the ultimate strength, crack starts to initiate, and therefore, the cohesive strength of the Ag-rich phase is equal to its ultimate strength, 155.7 MPa, and the cohesive strengths of the Sb-rich phase and $Ag_{30}Sb_{70}$ are equal to the yield strengths, 11.4 MPa and 17.94 MPa, respectively. The fracture toughness value of the Ag-rich phase is assumed to be 0.2 N/mm. The assumption was made due to the lack of material data in literature, and the assumed value falls within the range of pure Ag toughness values found in the literature.[30–32] Due to the brittleness of the Sb-rich phase and $Ag_{30}Sb_{70}$, the fracture toughness values are set to 0.0001 N/mm, simulating the brittle failure after the damage initiation.

The lamellar and monolithic $Ag_{30}Sb_{70}$ structures are shown in Supplementary Fig. 16. Li insertion was modeled with displacement-controlled boundary conditions to simulate dendrite growth. Periodic boundary conditions were applied along the top and bottom boundaries, and a uniform compressive stress of 20 MPa was applied horizontally. As shown in Supplementary Fig. 16B, in the monolithic $Ag_{30}Sb_{70}$ structure, crack propagation remains straight and horizontal during Li growth. In comparison, in Supplementary Fig. 16A, initially, the crack initiates and propagates following a straight path. After approaching the Ag-rich phase, crack deflection is seen, following the interface between the Ag-rich and Sb-rich phases.

The crack deflection mechanism in a bi-material system has been studied mathematically and numerically.[20,21] Whether a crack deflects along the bi-material interface or penetrates from one material to the other is determined jointly by the strain energy release rate ($SERR$) values of the

crack deflection case, $SERR_d$, and the crack penetration cases, $SERR_p$, and the fracture toughness values of the two materials.[20] The condition for crack deflection is,

$$\frac{\Gamma_i}{\Gamma_m} < \frac{SERR_d}{SERR_p} \quad (10)$$

where, $\boldsymbol{\Gamma_i}$ is the fracture toughness of the interface under appropriate mixed-mode conditions, and $\boldsymbol{\Gamma_m}$ is the fracture toughness of the material on the other side of the interface. The crack deflection mechanism and condition described in [20] are illustrated in Supplementary Fig. 17. Cohesive strengths of the bi-material system were later incorporated into crack deflection modeling, leveraging cohesive damage analysis.[21] Computational results indicate that whether a crack deflects or penetrates depends on both $\frac{\boldsymbol{\Gamma_i}}{\boldsymbol{\Gamma_m}}$ and $\frac{\boldsymbol{\hat{\sigma}_i}}{\boldsymbol{\hat{\sigma}_m}}$, where $\boldsymbol{\hat{\sigma}_i}$ is the cohesive strength of the interface and $\boldsymbol{\hat{\sigma}_m}$ is the cohesive strength of the material on the other side of the interface.[21] The parameter study further shows that a crack preferably deflects with smaller $\frac{\boldsymbol{\Gamma_i}}{\boldsymbol{\Gamma_m}}$ and $\frac{\boldsymbol{\hat{\sigma}_i}}{\boldsymbol{\hat{\sigma}_m}}$ values.[21] In this paper, an interface was not explicitly modeled between the Ag-rich and Sb-rich phases. Instead, the crack deflection was modeled as cracking in the Sb-rich phase along the interface. Therefore, in the analysis, due to the crack propagating in the Sb-rich phase, $\boldsymbol{\Gamma_i}$ and $\boldsymbol{\hat{\sigma}_i}$ are the fracture toughness and cohesive strength values of the Sb-rich phase. $\boldsymbol{\Gamma_m}$ and $\boldsymbol{\hat{\sigma}_m}$ are the fracture toughness and cohesive strength values of the Ag-rich phase. Accordingly, $\frac{\boldsymbol{\Gamma_i}}{\boldsymbol{\Gamma_m}}$ =0.0005 and $\frac{\boldsymbol{\hat{\sigma}_i}}{\boldsymbol{\hat{\sigma}_m}} = 0.073$, both are small and facilitate the deflection of the crack along the interface between the Ag-rich and Sb-rich phases.

Acknowledgement

H.Z. acknowledges the financial support received from the Office of Science Department of Energy under Award Number DESC0024528. This manuscript is partially based upon work supported by the U.S. Department of Energy's Office of Energy Efficiency and Renewable Energy (EERE) under the Bioenergy Technologies Office award number DE-EE0010296. This manuscript was partially authored by UT-Battelle LLC under contract DE-AC05-00OR22725 with DOE. The US government retains and the publisher, by accepting the article for publication, acknowledges that the US government retains a nonexclusive, paid-up, irrevocable, worldwide license to publish or reproduce the published form of this manuscript, or allow others to do so, for US government purposes. DOE will provide public access to these results of federally sponsored

research in accordance with the DOE Public Access Plan (http://energy.gov/downloads/doe-public-access-plan). This research was performed on APS beam time award(s) (DOI: https://doi.org/10.46936/APS-190733/60014598) from the Advanced Photon Source, a U.S. Department of Energy (DOE) Office of Science user facility at Argonne National Laboratory, and is based on research supported by the U.S. DOE Office of Science-Basic Energy Sciences, under Contract No. DE-AC02-06CH11357. Y.C. and B.P. acknowledge the financial support from the U.S. National Science Foundation (NSF) under Award Number 2038083.

Author contributions: H.Z. conceived and supervised this project. H.Z. and C.X designed the experiments. C.X conducted electrochemical tests. C.X. and J.W. performed SEM and XRD characterization, and C.X. analyzed the results. Y.C., S.L. and B.P conducted the simulation and drafted corresponding contents. H.Z. and L.L conducted XRF characterizations, and C.X. analyzed the results. X.Z and E.C. conducted XCT characterizations. C.X. analyzed XCT results. C.X. drafted the manuscript. H.S. and C.W. helped to revise the manuscript. All authors discussed the results, as well as the writing and revision of the manuscript.

Competing interests: There are no conflicts to declare.

Data and materials availability: All data associated with this work can be found in the main text or the supplementary information.

Reference

1. Kalnaus, S., Dudney, N. J., Westover, A. S., Herbert, E. & Hackney, S. Solid-state batteries: The critical role of mechanics. *Science.* **381**, 1300 (2023).
2. Meng, Y. S., Srinivasan, V. & Xu, K. Designing better electrolytes. *Science.* **378**, eabq3750 (2022).
3. Wang, T. *et al.* Fatigue of Li metal anode in solid-state batteries. *Science.* **388**, 311–316 (2025).
4. Fincher, C. D. *et al.* Electrochemical corrosion accompanies dendrite growth in solid electrolytes. *Nature* **652**, 906–911 (2026).
5. Doux, J. M. *et al.* Stack Pressure Considerations for Room-Temperature All-Solid-State Lithium Metal Batteries. *Adv. Energy Mater.* **10**, 1903253 (2020).
6. Ning, Z. *et al.* Dendrite initiation and propagation in lithium metal solid-state batteries. *Nature* **618**, 287–293 (2023).

7. Hu, X. *et al.* The role of grain boundaries in solid-state Li-metal batteries. *Nat. Rev. Mater.* **9**, 305–320 (2024).
8. Sandoval, S. E. *et al.* Electro-chemo-mechanics of anode-free solid-state batteries. *Nat. Mater.* **24**, 673–681 (2025).
9. Ye, L. & Li, X. A dynamic stability design strategy for lithium metal solid state batteries. *Nature* **593**, 218–222 (2021).
10. Zhang, Y. *et al.* Mechanically driven Li dendrite penetration in garnet solid electrolyte. *Nature* **652**, 912–918 (2026).
11. Cui, T. *et al.* Dendrite initiation and deflection in biaxially stressed solid electrolytes. *Nature* **655**, 631–637 (2026).
12. Ankem, S., Margolin, H., Greene, C. A., Neuberger, B. W. & Oberson, P. G. Mechanical properties of alloys consisting of two ductile phases. *Prog. Mater. Sci.* **51**, 632–709 (2006).
13. Manasijević, D. *et al.* Microstructure evaluation and thermal properties of Ag–Sb alloys. *Journal of Physics and Chemistry of Solids* **169**, 110874 (2022).
14. Vaughey, J. T., Fransson, L., Swinger, H. A., Edström, K. & Thackeray, M. M. Alternative anode materials for lithium-ion batteries: A study of Ag3Sb. *J. Power Sources* **119–121**, 64–68 (2003).
15. Gnanapoongothai, T., Murugan, R. & Palanivel, B. First-principle study on lithium intercalated antimonides Ag3Sb and Mg3Sb2. *Ionics (Kiel).* **21**, 1351–1361 (2015).
16. Wan, H., Wang, Z., Zhang, W., He, X. & Wang, C. Interface design for all-solid-state lithium batteries. *Nature* **623**, 739–744 (2023).
17. Zhu, C. *et al.* Understanding the evolution of lithium dendrites at Li6.25Al0.25La3Zr2O12 grain boundaries via operando microscopy techniques. *Nat. Commun.* **14**, 1300 (2023).
18. Zhang, B. *et al.* Atomic mechanism of lithium dendrite penetration in solid electrolytes. *Nat. Commun.* **16**, 1906 (2025).
19. Lee, S. *et al.* Design of a lithiophilic and electron-blocking interlayer for dendrite-free lithium-metal solid-state batteries. *Sci. Adv* **8**, 153 (2022).
20. Het, M.-Y. & Hutchinson, W. CRACK DEFLECTION AT AN INTERFACE BETWEEN DISSIMILAR ELASTIC MATERIALS. *Inl. J. Solids SlruClures* **25**, 1053–1067 (1989).
21. Parmigiani, J. P. & Thouless, M. D. The roles of toughness and cohesive strength on crack deflection at interfaces. *J. Mech. Phys. Solids* **54**, 266–287 (2006).

22. Kalarasse, L., Bennecer, B. & Kalarasse, F. Elastic and electronic properties of the alkali pnictide compounds Li 3Sb, Li3Bi, Li2NaSb and Li2NaBi. *Comput. Mater. Sci.* **50**, 2880–2885 (2011).
23. Li, J. H., Zhu, X. H., Cheng, Y. & Ji, G. F. Structural, electronic, elastic and thermal properties of Li2AgSb: First-principles calculations. *Zeitschrift fur Naturforschung - Section A Journal of Physical Sciences* **70**, 611–618 (2015).
24. Pant, B. R., Ren, Y. & Cao, Y. Dendrite Growth and Dead Lithium Formation in Lithium Metal Batteries and Mitigation Using a Protective Layer: A Phase-Field Study. *ACS Appl. Mater. Interfaces* **16**, 56947–56956 (2024).
25. Ren, Y., Zhou, Y. & Cao, Y. Inhibit of Lithium Dendrite Growth in Solid Composite Electrolyte by Phase-Field Modeling. *Journal of Physical Chemistry C* **124**, 12195–12204 (2020).
26. Yin, X. *et al.* Insights into morphological evolution and cycling behaviour of lithium metal anode under mechanical pressure. *Nano Energy* **50**, 659–664 (2018).
27. Goodfellow. Silver (Ag) material properties. *https://www.goodfellow.com/usa/material/precious-metals/silver*.
28. AZoM. Silver (Ag) – Material properties. *https://www.azom.com/properties.aspx?ArticleID=600*.
29. Papović, M. Significant characteristics of lead and alloys with antimony in the production of small arms ammunition. in 493–498 (11th International Scientific Conference on Defensive Technologies-OTEX 2024, 2024). doi:10.5937/oteh24088p.
30. Zhao, S. *et al.* On mode II fracture toughness of sintered silver based on end-notch flexure (ENF) test considering various sintering parameters. *Materials Science and Engineering: A* **823**, 141729 (2021).
31. Chen, C. *et al.* Macroscale and microscale fracture toughness of microporous sintered Ag for applications in power electronic devices. *Acta Mater.* **129**, 41–51 (2017).
32. Zhang, L., Elwazri, A. M., Zimmerly, T. & Brochu, M. Shear punch testing and fracture toughness of bulk nanostructured silver. *Mater. Des.* **30**, 1445–1450 (2009).

Supplementary Files

This is a list of supplementary files associated with this preprint. Click to download.

- SupportingInformationNatureNanotechnology.docx